Solution-Processed Graphene Quantum Dot Deep-UV Photodetectors

Qing Zhang,[†] Jiansheng Jie,[*,†] Senlin Diao,[†] Zhibin Shao,[†] Qiao Zhang,[†] Liu Wang,[†] Wei Deng,[†] Weida Hu,[‡] Hui Xia,[‡] Xiaodong Yuan,[†] and Shuit-Tong Lee[*,†]

[†]Institute of Functional Nano & Soft Materials (FUNSOM), Jiangsu Key Laboratory for Carbon-Based Functional Materials & Devices, Soochow University, Suzhou, Jiangsu 215123, P. R. China and [‡]National Laboratory for Infrared Physics, Shanghai Institute of Technical Physics, Chinese Academy of Sciences, Shanghai 200083, P. R. China

ABSTRACT Fast-response and high-sensitivity deep-ultraviolet (DUV) photodetectors with detection wavelength shorter than 320 nm are in high demand due to their potential applications in diverse fields. However, the fabrication processes of DUV detectors based on traditional semiconductor thin films are complicated and costly. Here we report a high-performance DUV photodetector based on graphene quantum dots (GQDs) fabricated via a facile solution process. The devices are capable of detecting DUV light with wavelength as short as 254 nm. With the aid of an asymmetric electrode structure, the device performance could be significantly improved. An on/off ratio of ~6000 under 254 nm illumination at a relatively weak light intensity of 42 μW cm^{-2} is achieved. The devices also exhibit excellent stability and reproducibility with a fast response speed. Given the solution-processing capability of the devices and extraordinary properties of GQDs, the use of GQDs will open up unique opportunities for future high-performance, low-cost DUV photodetectors.

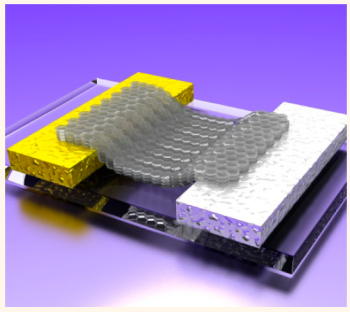

KEYWORDS: graphene · quantum dots · deep-UV · photodetectors · asymmetric electrodes

Deep-ultraviolet (DUV) photodetectors with detection wavelength shorter than 320 nm have been a subject of great interest due to their important applications in diverse fields, including remote control, chemical analysis, flame detection, ozone layer monitoring, missile warning system, and secure space-to-space communications.[1,2] Traditional DUV or ultraviolet (UV) detectors are made of semiconductor thin films with wide band gap, such as ZnO, GaN, and AlGaN, or silicon with an appropriate filter to render it visible-blind.[3] However, the fabrication processes for high-quality semiconductor thin films and DUV/UV detectors are complicated and costly. The detectors may also have lattice mismatch issues between the thin films and the substrates, which cause deterioration of device performance and result in poor long-term stability under DUV/UV irradiation.[4] Silicon photodiodes need high-temperature processing and also suffer from severe surface recombination due to strong surface light absorption at DUV range. Recently, one-dimensional (1D) semiconductor nanostructure-based DUV/UV detectors have attracted much attention due to high sensitivity arising from the surface effects.[1] Although various wide band gap semiconductor nanostructures, such as ZnO nanowires,[5] ZnS nanobelts,[6] Zn_2GeO_4 nanowires,[7] and Ga_2O_3 nanowires,[8] have been exploited for this purpose, the difficulties in nanostructure manipulation as well as device integration impede the large-scale applications of 1D nanostructures in DUV/UV detectors.

Because of the advantages of high chemical stability, earthly abundance, and nontoxicity, carbon-based materials have emerged as attractive candidates in the applications of bioimaging, catalysis, photovoltaics, and optoelectronic devices.[9] Graphene has a structure of two-dimensional sheet of carbon atoms, which has received tremendous interest in recent years because of its extraordinary electronic, optical, mechanical, and thermal properties.[9,10] Despite the excellent properties, graphene's zero band gap nature and semimetal conductivity have hindered its applications for which semiconducting properties of materials

* Address correspondence to jsjie@suda.edu.cn, apannale@suda.edu.cn.

Received for review October 27, 2014 and accepted January 27, 2015.

Published online January 27, 2015
10.1021/acsnano.5b00437

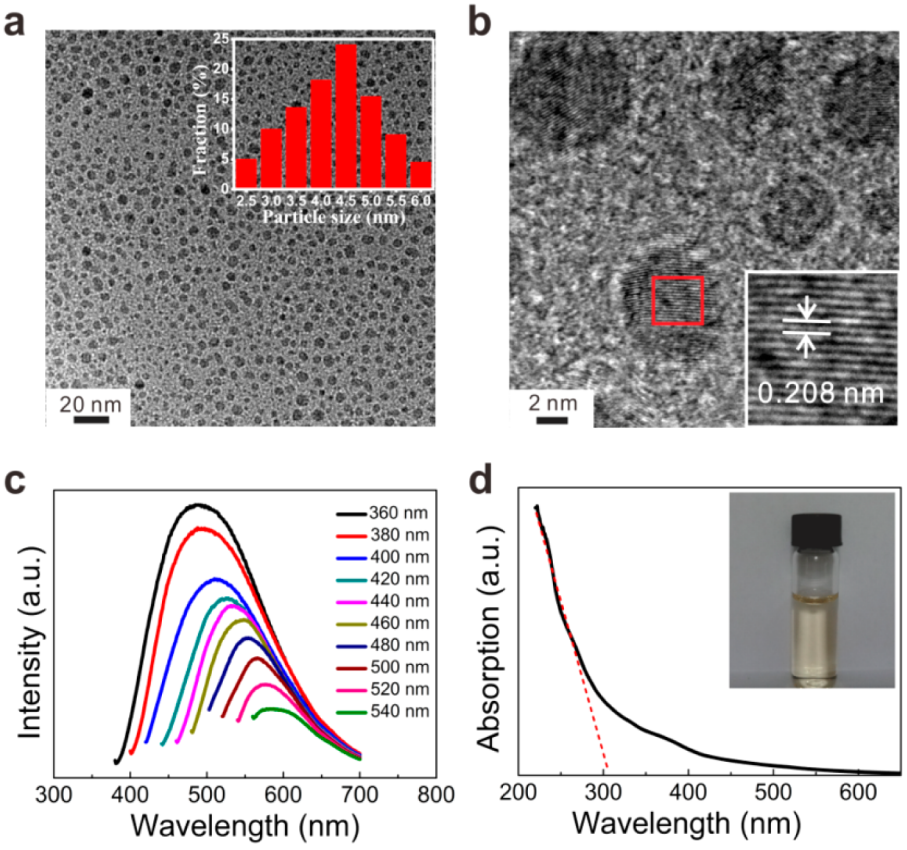

Figure 1. (a) TEM image of GQDs. Inset: size distribution diagram of GQDs. (b) HRTEM image of GQDs. Inset: the enlarged image from the red box in panel b. (c) PL spectra of GQDs under different excitation wavelengths. (d) UV−vis absorption spectrum of GQDs. The absorption edge is fitted by a dashed line. Inset: the photography of the aqueous solution of GQDs, showing light yellow color.

are desired. For instance, graphene absorbs light weakly over a broad wavelength range with no spectral selectivity, which limits its use as light-active material. Therefore, graphene-based photodetectors usually exhibit very low photoresponsivity, even though its photoresponse can be improved somewhat with the aid of surface plasma or surface modified semiconductor quantum dots.[11,12] There are a few ways to introduce band gap into graphene and one of the most efficient methods is to constrain graphene edges along two dimensions.[13] That is, shrinking the size of graphene until it turns to zero-dimensional (0D) quantum dots. To date, various methods have been developed to synthesize monodisperse and solution-stable graphene quantum dots (GQDs) of less than 10 nm, including hydrothermal method,[14] electrochemical strategies,[15] chemical exfoliation of carbon fibers,[16] solution chemistry method,[17] and ultrasonic and microwave method.[18] The band gap of GQDs is tunable in the UV to DUV range because of quantum confinement and edge effects.[19] Owing to a large optical absorptivity, tunable band gap, efficient multiple carrier generation, nontoxicity, high stability, and low cost,[13,20] GQDs have shown promising applications in photovoltaics and light-emitting diodes.[20−22]

Herein, we report a novel DUV photodetector fabricated from GQDs via a solution process. Because of the large band gap of GQDs, the devices were capable of detecting DUV light with wavelength as short as 254 nm. The role of device architecture was further exploited. By introducing an asymmetric electrode structure of Ag−Au, the photosensitivity of GQD-based photodetectors could be greatly enhanced by a factor of ~500 as compared with that of Au−Au symmetric electrodes. Besides, the devices exhibited excellent stability and reproducibility with a fast response speed. Our work demonstrates the great potential of GQDs as high performance, low-cost DUV photodetectors.

RESULTS AND DISCUSSION

GQDs used in this study are synthesized through a hydrothermal method developed by Pan and coworkers.[14] Figure 1a shows the low-magnification transmission electron microscopy (TEM) image of GQDs. The diameter of the dots is in the range of 2.5−6 nm, and the majority of dots have a size of 4−5 nm. From the atomic force microscopy (AFM) image of the GQDs (Figure S1, Supporting Information), the topographic heights are mostly between 0.4 and 2.5 nm, corresponding to 1−4 graphene layers.[23] The high-resolution TEM (HRTEM) image in Figure 1b reveals the GQDs are highly crystallized with the lattice spacing of 2.08 Å, which is in good agreement with the $(0\bar{1}10)$ plane of graphite.[24,25]

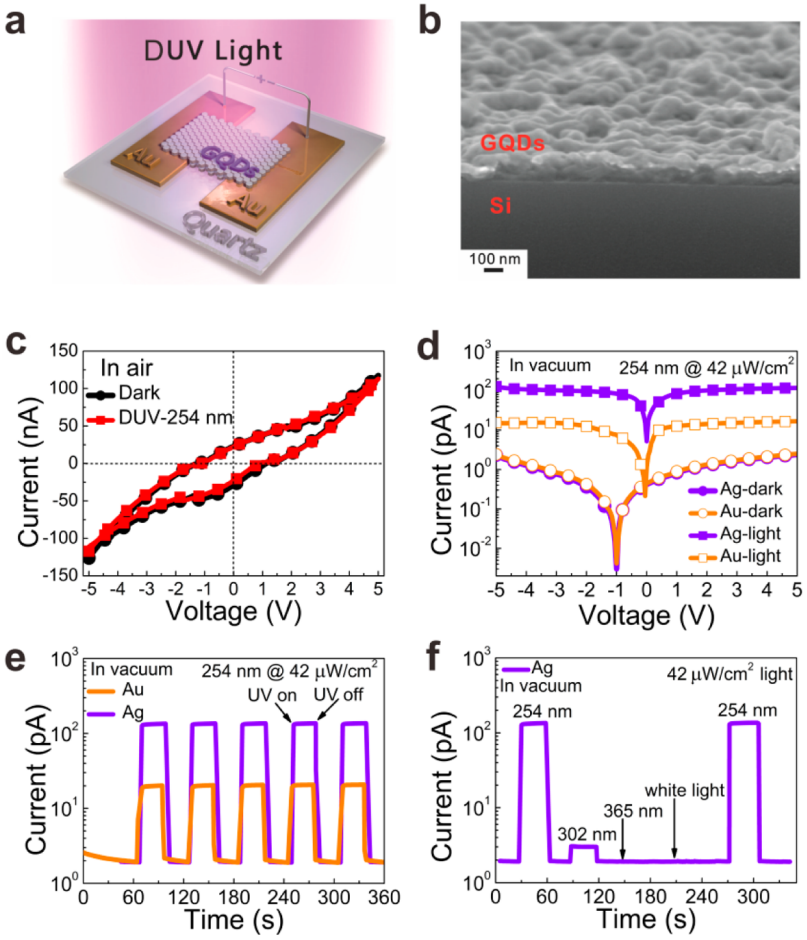

Figure 2. (a) Schematic illustration of the configuration for photoconductive measurements of GQDs with symmetric electrodes. (b) Cross-sectional SEM image of the GQD layer on silicon substrate. (c) Typical *I*−*V* curves of the GQD layer measured in the dark and under 254 nm light illumination (42 μW cm^{-2}), respectively, in air. (d) Semilogarithmic *I*−*V* curves of the devices with symmetric electrodes of Au−Au and Ag−Ag in dark and under 254 nm light illumination. The measurements were performed in vacuum (ca. 3.7 × 10^{-5} Torr). Time response of the devices with symmetric electrodes to (e) pulsed incident light and (f) light with different wavelengths. The voltage bias was fixed at +5 V during measurements.

As shown in Figure 1c, the PL spectra are broad with the peaks red-shifting from 485 to 580 nm, along with decreasing peak intensity, while the excitation wavelengths increase from 360 to 540 nm. The strongest PL peak appears at 485 nm upon 360 nm excitation. This excitation-dependent PL behavior is consistent with previous investigation on GQDs and has been extensively reported in fluorescent carbon-based nanomaterials.[24,26] The inhomogeneous orbital energy distribution of the defect states is suggested to be responsible for this phenomenon.[27,28] The inset in Figure 1d displays the photograph of the aqueous solution of GQDs, which is nearly transparent with light yellow color. Interestingly, the GQDs exhibit an intensive absorption at the DUV range, as evidenced by the UV−vis absorption spectrum (Figure 1d). The absorption onset is at ca. 320 nm by taking the intercept of the extrapolation of the absorption edge to the *x* axis. Therefore, as a rough estimation, the optical band gap of the GQDs can be estimated to be as large as ca. 3.8 eV.

Figure 2a illustrates the device configuration for the photoconductive measurements with symmetric electrodes. It is worth noting that the GQD-based photodetectors can be constructed via a facile solution process, in contrast to the complicated and expensive thin film growth process required for the traditional thin-film-based devices. In this process, the aqueous solution of GQDs was drop-casted into the device channel of prefabricated electrode pairs on quartz substrate and then dried at 70 °C for 15 min. The width and length of the device channel are 10 and 1 mm, respectively (Figure S2, Supporting Information). Figure 2b shows the cross-sectional SEM image of the GQD layer, which is uneven with an approximate thickness of 80 nm. The uneven layer can be mainly ascribed to the use of aqueous solution of GQDs: the evaporation of water under heating condition is nonuniform, which causes the local aggregation of the GQDs as well as the rough surface. To assess the effect of device architecture, devices with symmetric electrode pairs of both Au−Au and Ag−Ag were

investigated. Figure 2c depicts the typical current−voltage ($I-V$) characteristics of the device with Au−Au electrode pair in dark and under 254 nm DUV light illumination in air, respectively. The current was measured as a function of voltage swept from −5 to +5 V and then back. The $I-V$ curve exhibits a nonlinear characteristic with a significant hysteresis. The relatively large current at zero voltage proves a typical resistive switching existing in this device.[29,30] The currents at the same voltage are obviously different and the difference between the values of the forward and backward sweep at 0 V is about 51.9 nA. The distinct displacement at 0 A is about 2.31 V. The phenomenon of such a big hysteresis could be attributed to charge trapping in GQDs arising from the adsorbed oxygen or water molecules.[29] Similar phenomena have been observed in other nanomaterials such as ZnO nanowire and MoS_2 film.[31,32] Under DUV light illumination (Figure 2c), however, we find that the photoresponse of the GQD layer in air is nearly negligible. In most cases, the photocurrent even decreases slightly as compared to the dark current. This result can be ascribed to desorption of oxygen and water molecules adsorbed on GQDs' surface in air.[33,34] When the device is exposed to air in dark, the adsorbed oxygen and water molecules will be ionized by capturing free electrons from GQDs due to their strong electronegativity. Holes will then accumulate in GQDs during this process, leading to the higher conductivity of GQDs in air. Upon illuminating the device with DUV light, the photogenerated holes will migrate to the surface of GQDs and discharge the adsorbed water and oxygen molecules. At the same time, photogenerated electrons will recombine with the holes in the GQDs, eventually resulting in the decrease of GQD conductivity in the light.[35]

To assess the intrinsic transport characteristics of GQDs, the devices were further tested in vacuum (ca. 3.7×10^{-5} Torr), as shown in Figure 2d. Notably, the dark current decreases remarkably by almost 5 orders of magnitude from 125 nA to 2.4 pA at +5 V (Figure S3, Supporting Information). Desorption of surface-adsorbed oxygen and water molecules could be responsible for this result. The little literature addressing the transport properties of GQDs reported that GQDs showed p-type conductivity in air with a hole mobility as low as 0.01 $cm^2\ V^{-1}\ s^{-1}$, and the conduction current decreased by nearly 2 orders of magnitude after eliminating the surface-adsorbed water molecules by annealing in Ar.[36,37] This observation is in good agreement with our result. The high resistance, along with the low mobility, suggests that the carriers very likely transport via interdot hopping or tunnelling in the GQD film.

Significantly, after reducing the surface effect, the devices in vacuum exhibit much more pronounced photoresponse; the photocurrent increases by 13 times relative to the dark current for the device with Au−Au electrodes under 254 nm DUV light illumination at +5 V, while even higher increase of 90 times is achieved for the device with Ag−Ag electrodes. We note that the $I-V$ curves deflect from the origin, especially for the $I-V$ curves measured in the dark. This result is caused by the residual gas molecules adsorbed on GQD surface, which induce an obvious hysteresis for the curves even in vacuum (Figure S3, Supporting Information). From the time response curves in Figure 2e, it is noted that the response of the devices to pulsed light is quite stable with reasonable response speed. However, the accurate response time is limited by the temporal response of the preamp of the semiconductor parameter analyzer due to the very low current, as we will discuss later. Photoresponse of the device to the light with different wavelengths was also detected, as shown in Figure 2f. Significantly, the device is only sensitive to DUV light (302 and 254 nm), but fully blind to 365 nm light or white light. This result unambiguously demonstrates the great potential of GQDs as solar-blind DUV photodetectors.

To get deeper insight into the work mechanism of the GQD-based photodetectors, we studied the energy band diagrams of devices with different structures, as shown in Figure 3. The lowest unoccupied molecular orbital (LUMO) level of GQDs was determined to be 3.6 eV by the cyclic voltammetry (CV) measurement (Figure S4, Supporting Information), which is in accordance with previous reports.[17,20] Therefore, the highest occupied molecular orbital (HOMO) level of the GQDs can be estimated to be 7.4 eV by taking account of the optical band gap of GQDs (3.8 eV). When the metallic electrodes, e.g., Au with high work function (W_{Au}) of 5.1 eV, make contact with GQDs, a large Schottky barrier (Φ_{Bp}, ~2.3 eV) will exist at the Au/GQDs interface (Figure 3a). Upon DUV light irradiation with energy larger than the band gap, the electron−hole pairs, i.e., excitons, will be generated in GQDs. Note that the data for the exciton binding energy in GQDs is not available at the moment. However, it is reported that the exciton binding energies are 0.8−1.4 and 0.5−0.9 eV for armchair-edged graphene nanoribbons (AGNRs) with a width of 1.2 and 2.5 nm, respectively.[38,39] Considering the stronger spatial quantum confinement, the exciton binding energy in GQDs should be larger than that in AGNRs. Therefore, the exciton binding energy in GQDs is expected to be much larger than that in traditional inorganic semiconductors like Si (14.7 meV) and GaAs (4.2 meV), and be comparable to that in the organic electroluminescent (EL) materials (e.g., polydiacetylene (PDA) 500 meV, Tris (8-hydroxyquinolato) aluminum (Alq3) 1400 meV).[40] Owing to edge defects and surface potential arising from the adsorbed molecules, there is a large probability that the excitons will be dissociated at the GQD interface, and then the electrons and holes will drift toward the opposite electrodes under

the electric field, yielding the photocurrent. However, from the band energy diagram, we note that the electrons can freely drift to the anode, while a large barrier will exist at the cathode for hole transportation ($\Phi_{Bp}-V_2$). In contrast, in the case of Ag electrodes (Figure 3b), the barrier, $\Phi_{Bn}-V_1'$, will appear at the anode side for electron transportation, while the holes can drift freely, due to the lower work function of Ag (W_{Ag} = 4.26 eV). Since Φ_{Bn} (~0.66 eV) is much smaller than Φ_{Bp} (~2.3 eV), the carrier transportation barrier for Ag−Ag electrodes should be lower than that for Au−Au electrodes, leading to the substantially enhanced photocurrent in Ag−Ag device. Despite the increase of photocurrent by virtue of Ag−Ag electrodes, it is worth noting that the barrier will inevitably exist for the devices with symmetric electrodes, as confirmed by the analysis of energy band diagrams. In light of this, an asymmetric electrode structure is proposed in this study, i.e., Ag electrode serves as the cathode, while Au electrode serves as the anode, as illustrated in Figure 3c. In this case, both photogenerated electrons and holes can drift freely toward electrodes under forward bias direction. The carrier recombination will be effectively suppressed because the electron−hole pairs can be separated and transported readily. It is therefore expected that the photocurrent could be remarkably improved by taking advantage of the asymmetric electrode structure.

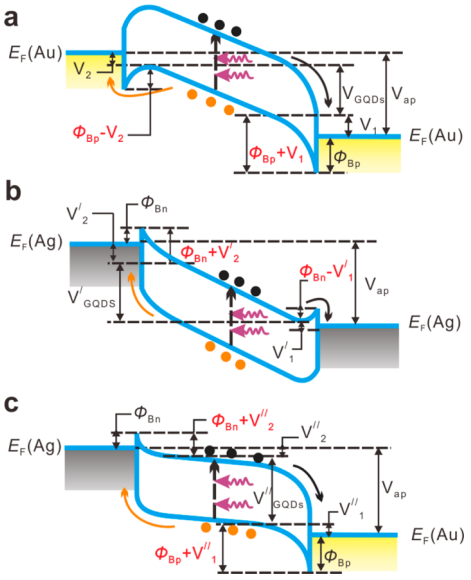

Figure 3. Energy band diagrams of GQD-based photodetectors with (a) Au−Au, (b) Ag−Ag, and (c) Ag−Au contacts, respectively. V_{ap} is the applied voltage, which is split between the two contacts. Positive bias is applied to the right and negative bias is applied to the left. E_F represents the Fermi level of the metals. V_{GQDs} (V'_{GQDs}, V''_{GQDs}) is the voltage drop in GQDs, V_1 (V'_1, V''_1) and V_2 (V'_2, V''_2) are the voltage drops at the forward and reverse contacts, respectively.

Figure 4a shows the schematic illustration of the device with asymmetric electrodes of Ag−Au. From the $I-V$ curves in Figure 4b, we note that the dark current is nearly in the same order with that of the devices with symmetric electrodes. However, the device exhibits a pronounced rectifying characteristic under light illumination due to the asymmetric electrode structure. The rectification ratio is about 20 at ±5 V under 254 nm light illumination. More importantly,

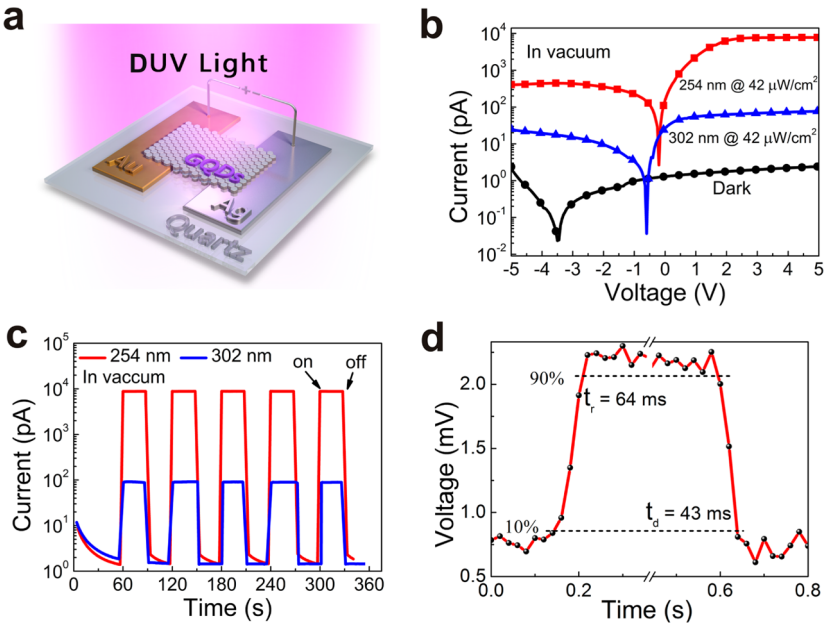

Figure 4. (a) Schematic illustration of the DUV photodetector with asymmetric Ag−Au electrodes. (b) $I-V$ curves of the device measured in the dark and under continuous 254 nm/302 nm DUV light (42 μW cm^{-2}) illumination. (c) Time response behavior of the device under pulsed 254 and 302 nm DUV light (42 μW cm^{-2}). The voltage bias was fixed at +5 V. (d) Enlarged rise and decay edges of the temporal response, which are measured by using a transimpedance amplifier with an oscilloscope. All the measurements were conducted in vacuum (ca. 3.7 × 10^{-5} Torr).

the photocurrent in the forward direction is dramatically improved as compared with that of the device with symmetric electrodes. Upon irradiating with 302 nm light, the photocurrent is 71.3 pA, which increases to 8823 pA under 254 nm light irradiation. Accordingly, the current on/off ratios (I_{light}/I_{dark}) of the Ag−Au device at +5 V are 48 and 5882 for 302 and 254 nm light, respectively, in contrast to the much smaller value of 1.2 (13) and 2 (90), respectively, for the Au−Au (Ag−Ag) device. From Figure 4c, it is evident that the GQDs can be reversibly switched between low and high conductivity; the device current increases sharply and stabilizes in a high-conductivity state upon light incidence and decreases quickly to a low-conductivity state after light illumination is turned off. For a photodetector, the rise time (t_r) is defined as the time interval for the response to rise from 10% to 90% of its peak value, whereas the decay time (t_d) is defined as the time interval for the response to decay from 90% to 10% of its peak value. Because of the low current of the device, the measurement of response time is actually limited by the semiconductor parameter analyzer. In order to precisely determine the response time, alternatively, we measured the temporal responses of the devices by using a transimpedance amplifier with an oscilloscope, as shown in Table 1. Notably, the Ag−Au device shows the fastest response speed with t_r and t_d of 64 and 43 ms (Figure 4d), respectively, indicating a rapid photoresponse characteristic of the device. To verify the durability of our devices, the DUV photodetector was tested again after storing in air for one month without any encapsulation (Figure S5, Supporting Information). The change in photoresponse is almost negligible, confirming the great durability of the device. The high chemical/physical stability of GQDs in air is likely responsible for the excellent durability of the device. Besides Ag, other metals with varied work functions, including In/Ga alloy (4.2 eV), Ti (4.33 eV), and Cu (4.65 eV) were also used to form electrode pairs with Au (Figure S6, Supporting Information). Obviously, the device performance is governed by the work function difference and enhanced with increasing work function difference, which is in line with the aforementioned device mechanism. Previous investigations on graphene photodetectors indicate that the photocurrent mainly comes from the metal−graphene interface.[41] Because of the short lifetimes of the photogenerated carriers in graphene sheet (in the ps range),[42] the absence of a strong electric field in the bulk graphene sheet will lead to carrier recombination without any contribution to the external photocurrent.[43] To understand the origin of photocurrent in GQD DUV photodetectors, we used a black light screen with a narrow slit (0.5 mm width) to shine 254 nm light at different positions of a Ag−Au device with a larger channel of 2 mm (Figure S7, Supporting Information). It is found that all these positions contribute to the photocurrent, although the photoresponses at the metal−GQD interfaces are indeed larger than that at the middle of a GQD film due to the stronger local built-in electric fields. The longer carrier lifetimes of GQDs compared to graphene sheet might be responsible for this result.

TABLE 1. Summary of the Key Parameters of GQD-Based DUV Photodetectors

electrode structures	I_{light}/I_{dark}	R_{max} (mA W^{-1})	D^* (cm Hz$^{1/2}$ W^{-1})	t_r (ms)	t_d (ms)
Ag−Au	5882	2.10	9.59×10^{11}	64	43
Ag−Ag	90	3.18×10^{-2}	1.45×10^{10}	128	102
Au−Au	13	4.26×10^{-3}	1.95×10^{9}	135	103

Generally, the key figure-of-merit parameters of responsivity (R) and detectivity (D^*) are used to evaluate the performance of a photodetector. R indicates how the efficiency of a detector responds to the optical signals and can be calculated according to the following equation:[44]

$$R = \frac{I_p}{P_{opt}} \tag{1}$$

where I_p is the photocurrent and P_{opt} is the incident light power (4.2×10^{-6} W). R is estimated to be 2.10 mA W^{-1} for Ag−Au device. In contrast, R is 3.18×10^{-2} and 4.26×10^{-3} mA W^{-1} for Ag−Ag and Au−Au devices (Table 1), respectively. However, D^* represents the ability of a detector to detect weak optical signals. If we assume that shot noise from dark current is the major contributor to the total noise, D^* can be expressed as[44]

$$D^* = \frac{(AB)^{1/2}}{NEP} \approx \frac{A^{1/2}R}{(2qI_d)^{1/2}} \tag{2}$$

where A is the area of the device (0.1 cm^2), B is the given bandwidth, and NEP is the noise equivalent power, which is a measure of the sensitivity of a photodetector and is defined as the signal power that gives a signal-to-noise ratio (SNR) of one, q is the elementary charge, and I_d is the dark current (1.5 pA). Accordingly, D^* are estimated to be 9.59×10^{11}, 1.45×10^{10}, and 1.95×10^9 cm Hz$^{1/2}$ W^{-1} for Ag−Au, Ag−Ag, and Au−Au devices (Table 1), respectively. In the above analysis, a shot noise limit is taken for the device to simplify the calculation. This may lead to the underestimation of the noise because other noise components, such as low-frequency noise (1/f noise), may also contribute to the total noise. Therefore, we directly measured the noise power density spectrum of the GQD DUV photodetector (Ag−Au device) within the frequency range from 1 to 1500 Hz, as shown in Figure S8 in the Supporting Information. It is noteworthy that the device shows low noise currents of <2 pA Hz$^{-1/2}$, which is smaller than that of a silicon diode (ca. 10 pA Hz$^{-1/2}$).[45]

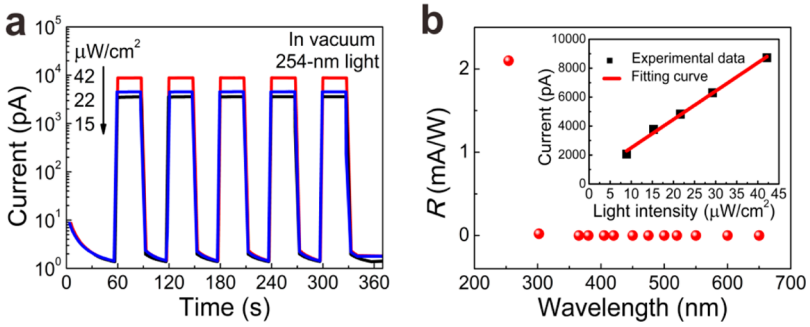

Figure 5. (a) Photoresponse of the device with Ag−Au electrodes under various 254 nm UV light intensities in vacuum. The voltage bias is fixed at +5 V. (b) Spectral responsivity of the DUV photodetector under +5 V bias. Inset: the dependence of photocurrent on light intensity under +5 V bias.

NEP is determined to be 4.86×10^{-10} W by integrating the noise power density spectrum, giving rise to a D^* of $\sim 2.06 \times 10^{10}$ cm $Hz^{1/2}$ W^{-1}. This value is comparable to that obtained from eq 2, indicating that the shot noise limit offers a satisfactory approximation to estimate the D^* here. Moreover, given a light absorption (α) of ~17.4% for the GQD film at 254 nm (Figure S9, Supporting Information), the internal quantum efficiency (IQE) (η) of the Ag−Au device is deduced to be 5.9% by the following equation:[46]

$$\eta = \frac{I_p hc}{\alpha P_{opt} q \lambda} = R\frac{hc}{\alpha q \lambda} \quad (3)$$

where h is the Planck constant (6.626×10^{-34} Js), c is the speed of light, and λ is the wavelength of the incident light (254 nm). Though R of 2.10 mA W^{-1} for the GQD DUV photodetector is still lower than R for the conventional silicon photodiode in UV range (ca. 140 mA W^{-1}) and the compound photodetectors such as GaN (ca. 100 mA W^{-1}),[3] it is higher than R for the ZnO quantum dot/graphene hybrid UV photodetector (1.7 mA W^{-1}).[47] In addition, D^* of the GQD DUV photodetector is close to those of the compound-semiconductor quantum-dot photodetectors.[48,49]

Figure 5a depicts the time response of the Ag−Au device obtained at varied incident light intensity. The maximum photocurrent increases almost linearly with increasing light intensity (inset in Figure 5b). Notably, our DUV detector exhibits an excellent capacity to detect very weak optical signals. Even under a weak incident light of 8 μW cm^{-2}, the I_{light}/I_{dark} ratio has already reached over 2000. Figure 5b shows the dependence of responsivity as a function of the light wavelength. It reveals the device only responds to the DUV light (≤302 nm) and is fully blind to the visible light, which is consistent with the result obtained from symmetric electrodes (Figure 2f). This result further confirms the great superiority of the GQDs as solar-blind DUV photodetectors.

For comparison with 2.5−6 nm GQDs, GQDs with larger sizes of 5−10 and 8−16 nm were also prepared by altering the ultrasonic times during the synthesis, as shown in Figure S10a−c in the Supporting Information. From the absorption spectra of the GQDs (Figure S10d), we can see that the absorption onset decreases and consequently the optical bandgap of the GQDs increases with decreasing GQD sizes. The time response behaviors of the devices fabricated from GQDs with different sizes, Figure S10e, indicate that the GQDs with smaller sizes offer higher DUV photoresponse. In addition, the spectral responses of the devices in Figure S10f reveal that all the devices are only sensitive to DUV light and almost blind to visible light, although the GQDs, particularly for the GQDs with large sizes, show the absorption tails in the visible light range (>400 nm). We speculate that the following reasons might be responsible for this observation: First, the edge states or surface states may contribute to the light absorption of GQDs in the long wavelength range. However, they have little contribution to the photocurrent because the carriers on these states are highly localized and will recombine shortly after generation. In contrast, the DUV light offers enough energy to excite the carriers to the LUMO energy level of the GQDs. The carriers can thus transport between adjacent GQDs efficiently via hopping. The strong light absorption of the GQDs at DUV range also ensures a high carrier concentration in the GQD film so that the carriers have a large probability to overcome the metal−GQDs contact barrier via thermal excitation. Second, with the increase of GQD size, the reduction of quantum confinement effect makes their functioning more like graphene sheet. However, it is known that a graphene sheet possesses very short lifetimes for the photogenerated carriers,[42] leading to a strong carrier recombination. As a result, the photoresponse decreases with increasing GQD size. Finally, from the absorption spectra (Figure S10d), the light absorption of large-size GQDs (5−10 and 8−16 nm GQDs) at the detection wavelengths (254 and 302 nm) is higher than that of the small-size GQDs (2.5−6 nm). This means a stronger surface absorption for the devices fabricated from large-size GQDs; the higher surface recombination will also result in a lower photocurrent.

Owing to the simple solution processing capability and extraordinary properties of GQDs, GQD-based DUV

photodetectors have the great potential to surpass conventional compound semiconductor-based photodetectors in terms of low cost, high stability, and improved performance. Various potential improvements of our GQD-based photodetector design can be envisioned including the implementation of an encapsulation layer on the GQD layer to allow the device working in air or the use of asymmetric electrodes with a larger work function difference to enhance carrier separation and transportation. It is also possible to combine GQDs with graphene transparent electrodes, enabling a low-cost, full-carbon device architecture. A higher photocurrent could be achieved by changing the device structure from planar structure to vertical structure; the channel length between electrodes could be remarkably reduced from 1 mm to several hundreds of nanometers, leading to much more efficient carrier transportation. The GQD-based photodetectors are also compatible with flexible substrates, such as polyethylene terephthalate (PET) or poly(etherimide) (PEI), due to the low-temperature and solution-processed device fabrication process.

CONCLUSIONS

In summary, we have demonstrated the construction of high-performance DUV photodetectors based on GQDs fabricated via a facile solution process. Owing to the large band gap of GQDs, the detectors can be operated in DUV wavelength range with responsivity increasing with decreasing light wavelength. The device performance could be significantly improved with the aid of an asymmetric electrode structure. In comparison with symmetric Au−Au or Ag−Ag electrodes, the use of asymmetric Ag−Au electrodes can result in the reduction of carrier transportation barriers, giving rise to a much enhanced device sensitivity. The GQD-based photodetectors exhibit superior performance in terms of excellent stability and reproducibility, fast response speed, and high durability. This work opens up the great opportunities of using GQDs in high-performance, low-cost DUV photodetectors.

METHODS

Material Preparation and Characterizations. GQDs used in this work were synthesized via a hydrothermal method.[14] Briefly, graphene oxide (GO) sheets were first prepared via improved Hummers' method,[50] and then graphene sheets (GSs) were obtained by deoxidization of the GO sheets in a tube furnace at 300 °C for 2 h in a nitrogen atmosphere. GSs (0.05 g) were oxidized in a mixed solution of H_2SO_4 (10 mL) and HNO_3 (30 mL) under mild ultrasonication. The mixture was then diluted with deionized (DI) water (250 mL) and filtered through a 0.22 μm microporous membrane to remove the residual acids. Purified oxidized GSs were redispersed in DI water, and the pH was tuned to 8 with NaOH. The suspension was transferred to a poly(tetrafluoroethylene) (Teflon) lined autoclave and heated at 200 °C for 10 h. The resulting black suspension was filtered through a 0.22 μm microporous membrane, and a brown filtered solution was separated. Eventually, the colloidal solution was further dialyzed in a dialysis bag (retained molecular weight: 3500 Da) to obtain the GQDs. The morphology and crystal structure of GQDs were determined by TEM (Philips CM300). The PL spectra were measured by a fluorescence spectrometer (Horiba Jobin Yvon Flworomax-4) with varied excitation light in the range of 360−540 nm. UV−vis spectrum was measured by a UV/vis spectrophotometer (Lambda 750). The morphology of GQD layer was investigated by SEM (Carl Zeiss, Supra 55), and the topographic height of the GQDs was characterized by AFM (Veeco, MultiMode V).

Device Fabrication and Measurements. Three different device architectures, including symmetric structures of Au−Au/Ag−Ag and asymmetric structure of Ag−Au, were adopted for the GQD-based DUV photodetectors. First, 50 nm electrodes (Au or Ag) were deposited on the far ends of a smooth quartz substrate by e-beam evaporation (Kurt J Lesker Company, PVD 75) with device channel width and length of 10 and 1 mm (Figure S2, Supporting Information), respectively. Then an appropriate amount of GQD aqueous solution (~120 mL), dispersed uniformly via ultrasonfication, was dropped into the channel to fully cover the channel. After being heated at 70 °C for about 15 min, the residual solvent was evaporated. The thickness of the GQD layer was ca. 80 nm. Photoconductive characteristics of the devices were measured in a vacuum probe station (Lakeshore, CRX-4K/CRTTP6) with a semiconductor characterization system (Keithley 4200). A UV lamp with different light wavelengths of 254, 302, and 365 nm was used as the UV light source, while a Xe lamp (300 W) was used to produce the semimonochromatic light in the visible range by using different wavelength filters. Temporal responses of the device were measured by using a transimpedance amplifier (NF, Li75A) with an oscilloscope (Tektronix, DPO7254C). Noise power spectrum of the Ag−Au device was analyzed by a low-noise current preamplifier (DL Instruments, DL1211) and a Dynamic Signal Analyzer (SRS, SR770) at room temperature.

Conflict of Interest: The authors declare no competing financial interest.

Supporting Information Available: Figure S1. AFM image and height distribution of the GQDs. Figure S2. Photographs of the GQD-based photodetectors with different electrode structures. Figure S3. Dark *I*−*V* curves of GQDs in high vacuum. Figure S4. Cyclic voltammetry (CV) curve of the GQDs. Figure S5. Stability of the GQD-based DUV photodetector. Figure S6. Temporal responses of the devices with different electrode pairs. Figure S7. Photoresponse of the device at different positions. Figure S8. Noise power spectrum of the Ag−Au device. Figure S9. UV−vis absorption spectrum of 2.5−6 nm GQD film. Figure S10. Photoresponse behaviors of devices fabricated from GQDs with different sizes. This material is available free of charge via the Internet at http://pubs.acs.org.

Acknowledgment. This work was supported by the National Basic Research Program of China (2012CB932400), the Major Research Plan of the National Natural Science Foundation of China (No. 91233110), the National Natural Science Foundation of China (No. 51172151), and a Project Funded by the Priority Academic Program Development of Jiangsu Higher Education Institutions. We also thank the support from Collaborative Innovation Center of Suzhou Nano Science and Technology.

REFERENCES AND NOTES

1. Peng, L.; Hu, L. F.; Fang, X. S. Low-Dimensional Nanostructure Ultraviolet Photodetectors. *Adv. Mater.* **2013**, *25*, 5321–5328.
2. Hatch, S. M.; Briscoe, J.; Dunn, S. A. Self-Powered ZnO-Nanorod/CuSCN UV Photodetector Exhibiting Rapid Response. *Adv. Mater.* **2013**, *25*, 867–871.

3. Monroy, E.; Omnes, F.; Calle, F. Wide-Bandgap Semiconductor Ultraviolet Photodetectors. *Semicond. Sci. Technol.* **2003**, *18*, R33–R51.
4. Liang, H. L.; Mei, Z. X.; Hou, Y. N.; Liang, S.; Liu, Z. L.; Liu, Y. P.; Li, J. Q.; Du, X. L. Realization of W−MgZnO Epitaxial Growth on BeO-Buffered ZnO for UV-B Photodetectors. *J. Cryst. Growth* **2013**, *381*, 6–9.
5. Liu, X.; Gu, L. L.; Zhang, Q. P.; Wu, J. Y.; Long, Y. Z.; Fan, Z. Y. All-Printable Band-Edge Modulated ZnO Nanowire Photodetectors with Ultra-High Detectivity. *Nat. Commun.* **2014**, *5*, 4007.
6. Fang, X. S.; Bando, Y.; Liao, M. Y.; Zhai, T. Y.; Gautam, U. K.; Li, L.; Koide, Y.; Golberg, D. An Efficient Way to Assemble ZnS Nanobelts as Ultraviolet-Light Sensors with Enhanced Photocurrent and Stability. *Adv. Funct. Mater.* **2010**, *20*, 500–508.
7. Yan, C. Y.; Singh, N.; Lee, P. S. Wide-Band Gap Zn_2GeO_4 Nanowire Networks as Efficient Ultraviolet Photodetectors with Fast Response and Recovery Time. *Appl. Phys. Lett.* **2010**, *96*, 053108.
8. Li, Y.; Tokizono, T.; Liao, M. Y.; Zhong, M. A.; Koide, Y.; Yamada, I.; Delaunay, J. J. Efficient Assembly of Bridged β-Ga_2O_3 Nanowires for Solar-Blind Photodetection. *Adv. Funct. Mater.* **2010**, *20*, 3972–3978.
9. Castro Neto, A. H.; Peres, N. M. R.; Novoselov, K. S.; Geim, A. K. The Electronic Properties of Graphene. *Rev. Mod. Phys.* **2009**, *81*, 109–162.
10. Geim, A. K. Graphene: Status and Prospects. *Science* **2009**, *324*, 1530–1534.
11. Liu, Y.; Cheng, R.; Liao, L.; Zhou, H. L.; Bai, J. W.; Liu, G.; Liu, L. X.; Huang, Y.; Duan, X. F. Plasmon Resonance Enhanced Multicolour Photodetection by Graphene. *Nat. Commun.* **2011**, *2*, 579.
12. Konstantatos, G.; Badioli, M.; Gaudreau, L.; Osmond, J.; Bernechea, M.; de Arquer, F. P. G.; Gatti, F.; Koppens, F. H. L. Hybrid Graphene-Quantum Dot Phototransistors with Ultrahigh Gain. *Nat. Nanotechnol.* **2012**, *7*, 363–368.
13. Li, Y.; Hu, Y.; Zhao, Y.; Shi, G. Q.; Deng, L. E.; Hou, Y. B.; Qu, L. T. An Electrochemical Avenue to Green-Luminescent Graphene Quantum Dots as Potential Electron-Acceptors for Photovoltaics. *Adv. Mater.* **2011**, *23*, 776–780.
14. Pan, D. Y.; Zhang, J. C.; Li, Z.; Wu, M. H. Hydrothermal Route for Cutting Graphene Sheets into Blue-Luminescent Graphene Quantum Dots. *Adv. Mater.* **2010**, *22*, 734–738.
15. Lu, J.; Yang, J. X.; Wang, J. Z.; Lim, A. L.; Wang, S.; Loh, K. P. One-Pot Synthesis of Fluorescent Carbon Nanoribbons, Nanoparticles, and Graphene by the Exfoliation of Graphite in Ionic Liquids. *ACS Nano* **2009**, *3*, 2367–2375.
16. Peng, J.; Gao, W.; Gupta, B. K.; Liu, Z.; Romero-Aburto, R.; Ge, L.; Song, L.; Alemany, L. B.; Zhan, X.; Gao, G.; Vithayathil, S. A.; Kaipparettu, B. A.; Marti, A. A.; Hayashi, T.; Zhu, J. J.; Ajayan, P. M. Graphene Quantum Dots Derived from Carbon Fibers. *Nano Lett.* **2012**, *12*, 844–849.
17. Pan, D. Y.; Xi, C.; Li, Z.; Wang, L.; Chen, Z. W.; Lu, B.; Wu, M. H. Electrophoretic Fabrication of Highly Robust, Efficient, and Benign Heterojunction Photoelectrocatalysts Based on Graphene-Quantum-Dot Sensitized TiO_2 Nanotube Arrays. *J. Mater. Chem. A* **2013**, *1*, 3551–3555.
18. Zhuo, S. J.; Shao, M. W.; Lee, S. T. Upconversion and Downconversion Fluorescent Graphene Quantum Dots: Ultrasonic Preparation and Photocatalysis. *ACS Nano* **2012**, *6*, 1059–1064.
19. Yan, X.; Cui, X.; Li, L. S. Synthesis of Large, Stable Colloidal Graphene Quantum Dots with Tunable Size. *J. Am. Chem. Soc.* **2010**, *132*, 5944–5945.
20. Gupta, V.; Chaudhary, N.; Srivastava, R.; Sharma, G. D.; Bhardwaj, R.; Chand, S. Luminscent Graphene Quantum Dots for Organic Photovoltaic Devices. *J. Am. Chem. Soc.* **2011**, *133*, 9960–9963.
21. Gur, I.; Fromer, N. A.; Geier, M. L.; Alivisatos, A. P. Air-Stable All-Inorganic Nanocrystal Solar Cells Processed from Solution. *Science* **2005**, *310*, 462–465.
22. Luk, C. M.; Tang, L. B.; Zhang, W. F.; Yu, S. F.; Teng, K. S.; Lau, S. P. An Efficient and Stable Fluorescent Graphene Quantum Dot−Agar Composite as a Converting Material in White Light Emitting Diodes. *J. Mater. Chem.* **2012**, *22*, 22378–22381.
23. Xue, M. Q.; Chen, G. F.; Yang, H. X.; Zhu, Y. H.; Wang, D. M.; He, J. B.; Cao, T. B. Superconductivity in Potassium-Doped Few-Layer Graphene. *J. Am. Chem. Soc.* **2012**, *134*, 6536–6539.
24. Tang, L. B.; Ji, R. B.; Cao, X. K.; Lin, J. Y.; Jiang, H. X.; Li, X. M.; Teng, K. S.; Luk, C. M.; Zeng, S. J.; Hao, J. H.; Lau, S. P. Deep Ultraviolet Photoluminescence of Water-Soluble Self-Passivated Graphene Quantum Dots. *ACS Nano* **2012**, *6*, 5102–5110.
25. Pan, D. Y.; Guo, L.; Zhang, J. C.; Xi, C.; Xue, Q.; Huang, H.; Li, J. H.; Zhang, Z. W.; Yu, W. J.; Chen, Z. W.; Li, Z.; Wu, M. H. Cutting sp^2 Clusters in Graphene Sheets into Colloidal Graphene Quantum Dots with Strong Green Fluorescence. *J. Mater. Chem.* **2012**, *22*, 3314–3318.
26. Lingam, K.; Podila, R.; Qian, H. J.; Serkiz, S.; Rao, A. M. Evidence for Edge-State Photoluminescence in Graphene Quantum Dots. *Adv. Funct. Mater.* **2013**, *23*, 5062–5065.
27. Riggs, J. E.; Guo, Z. X.; Carroll, D. L.; Sun, Y. P. Strong Luminescence of Solubilized Carbon Nanotubes. *J. Am. Chem. Soc.* **2000**, *122*, 5879–5880.
28. Li, F. S.; Kou, L. J.; Chen, W.; Wu, C. X.; Guo, T. L. Enhancing the Short-Circuit Current and Power Conversion Efficiency of Polymer Solar Cells with Graphene Quantum Dots Derived from Double-Walled Carbon Nanotubes. *NPG Asia Mater.* **2013**, *5*, e60.
29. Kalita, H.; Harikrishnan, V.; Shinde, D. B.; Pillai, V. K.; Aslam, M. Hysteresis and Charge Trapping in Graphene Quantum Dots. *Appl. Phys. Lett.* **2013**, *102*, 143104.
30. Kou, L. J.; Li, F. S.; Chen, W.; Guo, T. L. Synthesis of Blue Light-Emitting Graphene Quantum Dots and their Application in Flexible Nonvolatile Memory. *Org. Electron.* **2013**, *14*, 1447–1451.
31. Maeng, J.; Park, W.; Choe, M.; Jo, G.; Kahng, Y. H.; Lee, T. Transient Drain Current Characteristics of ZnO Nanowire Field Effect Transistors. *Appl. Phys. Lett.* **2009**, *95*, 123101.
32. Late, D. J.; Liu, B.; Matte, H. R.; Dravid, V. P.; Rao, C. Hysteresis in Single-Layer MoS_2 Field Effect Transistors. *ACS Nano* **2012**, *6*, 5635–5641.
33. Yang, Y. X.; Murali, R. Binding Mechanisms of Molecular Oxygen and Moisture to Graphene. *Appl. Phys. Lett.* **2011**, *98*, 093116.
34. Ryu, S.; Liu, L.; Berciaud, S.; Yu, Y. J.; Liu, H. T.; Kim, P.; Flynn, G. W.; Brus, L. E. Atmospheric Oxygen Binding and Hole Doping in Deformed Graphene on a SiO_2 Substrate. *Nano Lett.* **2010**, *10*, 4944–4951.
35. Zhang, X. W.; Jie, J. S.; Wang, Z.; Wu, C. Y.; Wang, L.; Peng, Q.; Yu, Y. Q.; Jiang, P.; Xie, C. Surface Induced Negative Photoconductivity in P-type ZnSe: Bi Nanowires and their Nano-Optoelectronic Applications. *J. Mater. Chem.* **2011**, *21*, 6736–6741.
36. Kalita, H.; Harikrishnan, V.; Aslam, M. Field Effect Transport Properties of Electrochemically Prepared Graphene Quantum Dots. *2013 IEEE 5th Int. Nanoelectron. Conf. (INEC)* **2013**, 463–465.
37. Kalita, H.; Harikrishnan, V.; Aslam, M. High I_{on}/I_{off} Ratio of Electrochemically Prepared Graphene Quantum Dots. *AIP Conf. Proc.* **2013**, *1536*, 189–190.
38. Li, Y.; Marvin, L. C.; Steven, G. L. Excitonic Effects in the Optical Spectra of Graphene Nanoribbons. *Nano Lett.* **2007**, *7*, 3112–3115.
39. Zhu, X.; Su, H. B. Scaling of Excitons in Graphene Nanoribbons with Armchair Shaped Edges. *J. Phys. Chem. A* **2011**, *115*, 11998–12003.
40. Knupfer, M. Exciton Binding Energies in Organic Semiconductors. *Appl. Phys. A: Mater. Sci. Process.* **2003**, *77*, 623–626.
41. Sun, D.; Aivazian, G.; Jones, A. M.; Ross, J. S.; Yao, W.; Cobden, D.; Xu, X. D. Ultrafast Hot-Carrier-Dominated Photocurrent in Graphene. *Nat. Nanotechnol.* **2012**, *7*, 114–118.
42. Xia, F. N.; Mueller, T.; Golizadeh-Mojarad, R.; Freitag, M.; Lin, Y. M.; Tsang, J.; Perebeinos, V.; Avouris, P. Photocurrent Imaging and Efficient Photon Detection in A Graphene Transistor. *Nano Lett.* **2009**, *9*, 1039–1044.

43. Mueller, T.; Xia, F. N.; Avouris, P. Graphene Photodetectors for High-Speed Optical Communications. *Nat. Photonics.* **2010**, *4*, 297–301.
44. Wu, D.; Jiang, Y.; Zhang, Y.; Li, J. W.; Yu, Y. Q.; Zhang, Y. P.; Zhu, Z. F.; Wang, L.; Wu, C. Y.; Luo, L. B.; Jie, J. S. Device Structure-Dependent Field-Effect and Photoresponse Performances of P-type ZnTeSb Nanoribbons. *J. Mater. Chem.* **2012**, *22*, 6206–6212.
45. Malik, S.; Ray, A. K.; Bruce, S. 1/f Noise in Langmuir–Blodgett Films on Silicon. *Semicond. Sci. Technol.* **2005**, *20*, 453–458.
46. Yu, H. J.; Bao, Z. N.; Oh, J. H. High-Performance Phototransistors Based on Single-Crystalline n-Channel Organic Nanowires and Photogenerated Charge-Carrier Behaviors. *Adv. Funct. Mater.* **2013**, *23*, 629–639.
47. Son, D. I.; Yang, H. Y.; Kim, T. W.; Park, W., II. Photoresponse Mechanisms of Ultraviolet Photodetectors Based on Colloidal ZnO Quantum Dot-Graphene nanocomposites. *Appl. Phys. Lett.* **2013**, *102*, 021105.
48. Konstantatos, G.; Sargent, E. H. Nanostructured Materials for Photon Detection. *Nat. Nanotechnol.* **2010**, *5*, 391–400.
49. Lee, J. S.; Kovalenko, M. V.; Huang, J.; Chung, D. S.; Talapin, D. V. Band-Like Transport, High Electron Mobility and High Photoconductivity in All-Inorganic Nanocrystal arrays. *Nat. Nanotechnol.* **2011**, *6*, 348–352.
50. Sun, Y. Q.; Wang, S. Q.; Li, C.; Luo, P. H.; Tao, L.; Wei, Y.; Shi, G. Q. Large Scale Preparation of Graphene Quantum Dots from Graphite with Tunable Fluorescence Properties. *Phys. Chem. Chem. Phys.* **2013**, *15*, 9907–9913.